Measuring NMR and developing 2D imaging in a low-cost, portable MRI prototype

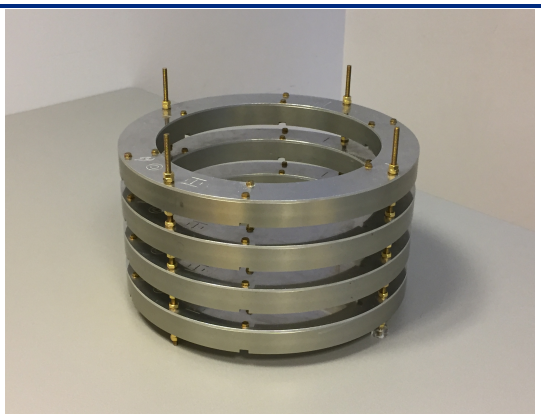

THESIS

submitted in partial fulfillment of the
requirements for the degree of

MASTER OF SCIENCE
in
PHYSICS

Author :	Roel Burgwal BSc
Student ID :	1307363
Supervisor :	prof. dr. Andrew G. Webb
2^{nd} corrector :	prof. dr. ir. Tjerk H. Oosterkamp

Leiden, The Netherlands, June 15, 2018

Measuring NMR and developing 2D imaging in a low-cost, portable MRI prototype

Roel Burgwal BSc

C.J. Gorter Center for High Field MRI, Leiden University Medical Center (LUMC)
Albinusdreef 2, 2333 ZA Leiden

June 15, 2018

Abstract

The medical technique of Magnetic Resonance Imaging (MRI) is barely available in developing countries because of its high cost and the strong requirements on infrastructure. To address this problem, we are developing a permanent magnet-based head scanner that is affordable ($<$ €50,000) and portable. Here, we report on the first observations of magnetic resonance in our custom magnet array with a field strength of 59 mT. Using custom made volume coils, we observe using Hahn echo (Spin echo) and CPMG pulse sequences. We discuss the step towards 2D imaging using rotating spatially encoding magnetic fields (rSEMs) and show simulations that indicate this is feasible in our setup. Finally, we discuss the technical challenges that still have to be overcome to turn this prototype into a diagnostic device for those in need.

Contents

Chapter 1

Introduction

1.1 MRI for the developing world

In a modern hospital, Magnetic Resonance Imaging (MRI) is a indispensable method for diagnosing. It offers imaging with good soft-tissue contrast, without the health hazard of ionising radiation that is applied during a CT scan. It can be used for numerous goals, for example, to find tumors, diagnose neurological disorders or find tears in joint ligament after injury [1].

The scanner makes use of the principle of Nuclear Magnetic Resonance (NMR). During a scan, the patient is placed in a magnetic field. Using radiofrequency (RF) pulses, the (hydrogen) atoms inside the patient can be excited and their subsequent relaxation measured. By collecting hydrogen relaxation signals throughout the body, a three-dimensional image can be constructed.

To perform this amazing feat, a scanner uses some sophisticated hardware. First, a strong magnetic field is generated by a superconducting coil. To make the coil superconducting, it is kept at only a few Kelvin by a liquid helium-based cooling system. Next, several coils are required to produce and capture RF signals. The high-power input of these coils is produced by RF amplifiers. Besides that, in traditional imaging, several more coils are needed to produce additional magnetic fields, called gradient fields. These coils each require strong and stable power sources. The whole of this setup needs to be shielded from external RF noise, which is often done by incorporating metal shielding in the room's walls. All in all, an MRI system is big, heavy and expensive. The price is most strongly dependent on the magnetic field strength, and is often quoted to be about 1M$ per Tesla, with conventional systems being mostly 1.5 or 3 T.

Because of these practical issues, MRI scans are often not available in developing countries. Besides the obvious issue of costs, other factors such as poor infrastructure (unreliable power supply) and lack of experience in operating and maintaining the equipment make running an MRI system a challenge in these countries. Additionally, the current systems cannot be transported, which also limits their effectiveness.

There is, however, a need for MRI scans in the treatment of diseases that affect many, such as hydrocephalus. Hydrocephalus affects many newly born in Africa, where there are an estimated 180,000 new cases every year in Sub-Saharan Africa [2]. For these children, hydrocephalus can be deadly or cause irreversible damage. MRI scanners could aid the surgical treatment [3], even if they would only have a relatively low resolution [4].

1.2 An overview of low-cost scanners in development

It is clear there is a need for low-cost and portable scanners. To realise this, the hardware of a scanner needs to be seriously redesigned. Inevitably a low-cost scanner has a much weaker static magnetic field (B_0) than conventional scanners, because the superconducting electromagnets will have to be replaced by either conventional electromagnets or permanent magnets. This in turn results in a strong decrease of signal that is received from the object one tries to image, which is the main challenge of building a low-cost MRI scanner. Additionally, one may also consider replacing the gradient coils used for 3D imaging by other imaging hardware. We will describe how several projects attempt to overcome these issues and then, in the next section, explain how our research fits in.

One approach to low-field scanners is to generate the B_0 field using large, non-superconducting coils. These produce weak, but homogeneous fields. One example is a 6.5 mT scanner with conventional gradient fields that performed a full head scan in 6 minutes with $2.5\times3.5\times8.5$ mm resultion [5, 6]. The short scan time was achieved by using special imaging sequences. This scanner performs well and is certainly much cheaper than conventional scanners. However, it is not very portable. The setup in contained in a large chamber that serves as a Faraday cage. The 2 meter diameter B_0 and gradient coils weigh around 700 kg altogether. Moreover, the stability of the B_0 field depends on DC power supplies that have a stability on the order of tens of ppm at 40 A of current. It is not clear whether

this stability can be maintained with the unreliable AC power supply of developing countries. The dissipative heat production in the coils is about 6 kW and cooling systems require an additional 2 kW, which means the setup requires a lot of power to run.

A way to improve the signal-to-noise ratio (SNR) in a low-field system is so-called pre-polarisation [7]. This involves an additional magnetic field, the pre-polarising field, in addition to the B_0 field. The idea is that the pre-polarising field, being stronger than the B_0 field, is applied before a measurement to increase the net magnetisation. It is then turned off, and a measurement is performed using the B_0 field. The advantage of this approach is that the homogeneity requirements on the pre-polarising field are much weaker, making it easier to achieve higher magnetisation without facing the consequences of inhomogeneity. This approach is used in the development of portable MRI by a group at Penn State University [4, 8]. This method, however, is also not without challenges. High power consumption may be a problem [8], as well as magnetic induction due to fast switching of the strong pre-polarising field.

Next, there are several projects that try to develop a scanner that uses permanent magnets in a Halbach array, which is similar to the approach we are taking. Most notably, Cooley et al. [9, 10] have published several papers describing their portable, low-cost MRI. The scanner succesfully produces 2D images by rotating the B_0 field around the sample. This imaging technique will be discussed further in chapter 5. We consider reproducing this 2D imaging an important milestone in the development of our own scanner. Another research project, based mainly at the Singapore University of Technology and Design, follows a similar path and uses permanent magnets and rotation for imaging [11, 12], although using a different reconstruction algorithm [13]. At the Berlin Ultra-high Field Facility, work is also being done on low-cost imaging using Halbach arrays [14, 15].

1.3 About this project

The aim of this project is to develop a low-cost (less than €50,000), portable MRI-scanner. The scanner will be designed to image the head and will thus not be a full-body scanner. Many projects, such as the Penn State pre-polarised scanner and all Halbach-based scanners, aim for the same goal, because it is easier to achieve than a full-body scanner and already has numerous applications.

Our approach will initially follow the same steps as the design by Cooley

et al., using a rotating Halbach array to perform 2D encoding. However, we aim to do this in a FOV large enough for the clinical application, which should be larger than the 14-cm sphere used in the demonstration by Cooley *et al.*. More importantly, the main outstanding challenge is that 3D imaging has not been demonstrated in this design and it is not yet clear what method would be feasible to do this. Another major challenge will be to reduce the scan time, which is in a trade-off with the resolution and quality of the scan.

These days, computational power comes cheap and is easily replacable. To exploit this, we are working together with the applied mathematics department of the TU Delft. The researchers here are working on image reconstruction methods for the signals that are produced by our low-field scanner with weak signal [16]. Next to that, they are looking at super-resolution reconstruction, where several low-resolution images are combined to produce one high-resolution image [17]. In summary, this research aims to make the requirement on low-field hardware less stringent by using more computational power and cleverly designed algorithms.

This project is part of the Open-Source Imaging Initiative*. This means that all hardware designs and software are to become openly available.

1.4 The contents of this thesis

This thesis describes one of the first steps in this project. It uses the work described in two previous theses [19, 20] to perform the first measurements of spin echoes. To do this, we used a Halbach array cylinder with a head-sized bore and a centre field strength of about 59 mT. We used both a single and two separate coils to perform the measurements. A custom made amplifier is used as well as a commercially available analogue-digital interface.

We discuss this in the following chapters:

1. **Introduction**

2. **Theory of low-field MRI**. Here, we calculate how expected SNR decreases as we decrease the B_0 field. Also, we show how one can describe the performance of coils at low field by means of a magnetostatic approximation.

*For more information, see [18] or visit `www.opensourceimaging.org`

Version of June 15, 2018– Created June 15, 2018 - 16:52

3. **Materials and methods**. The hardware is described extensively. We elaborate on what aspects one has to consider in designing a piece of hardware for low-field MRI.

4. **Magnetic resonance measurements**. Here, we show the first spin echo measurements for different coils and discuss how the results compare to our predictions. Also, we show the first CPMG measurements, in which we determine T_2 times for water and oil. Finally, we compare how our coil designs behave in experiment to what we expect from theory.

5. **Developing 2D imaging with rSEMs**. We describe the technique using rotating spatial encoding magnetic fields (rSEMs) that we plan on using for 2D imaging and perform simulations that show that this approach can work with our current B_0 field as rSEM.

6. **Future considerations**. Improvements need to be made to our setup to reach the required sensitivity with a short scan time. What do we intend to change in the near future? Moreover, additional changes need to be made to enable 3D imaging. What are possible approaches to doing this?

7. **Conclusions**.

Chapter 2

Theory of low-field MRI

In this chapter we will highlight those aspects of MRI that significantly change when moving from high to low magnetic fields. We will discuss the advantages and disadvantages this brings. Finally, we describe the behaviour of transmit coils at low-field, which can be done using a magnetostatic approximation.

2.1 Advantages of low-field

There are several reasons to use weak magnetic fields, the most important being cost and portability, which have been described in the introduction. Here, we will discuss some additional arguments from physics to choose for low-field.

The most important physical advantage is the long wavelength associated with our low Lamor frequency: $\lambda = \frac{c}{f} \approx 120$ m for the 59 mT field we use. This fact makes RF design easier in several ways. A long wavelength allows us to neglect the effect of distances in our electrical circuitry. Cables with a length of approximately a meter do not influence the behaviour of electronics as they would if the wavelength was of the order of a meter, in which case they could completely change impedances. In addition to that, we are able to make the magnetostatic approximation by using Biot-Savart equation when calculating the magnetic fields generated by our coils [21], as we will do in the final section of this chapter. This greatly simplifies calculations. Finally, having a wavelength in tissue that is comparable to patient body size allows for B_1 interference patterns [22]. This effect is present at high field, but much less strong at low ($<$0.2 T) fields [23].

Although MRI is considered safe, in contrast to X-ray and CT scans,

as it does not expose the patient to ionising radiation, energy from the RF pulses can still be absorbed by the patient. Therefore, a maximum allowed absorbed dose of RF has been set to ensure there are no detrimental effects to patient health. The absorbed dose is expressed in the Specific Absorption Rate (SAR), which is the absorbed power per unit mass. At high fields, the maximum SAR limits the rate at which pulses can be applied and gradient fields can be switched, but at low fields (<100 mT), this limit is much less stringent [24]. This is because the electric fields in the body are much smaller at lower frequencies, meaning less current and less absorption.

2.2 The decrease of signal strength

The main disadvantage of low-field MRI is that the available signal decreases as the B_0 field decreases. The signal strength depends on the induced electromotive force (EMF) by the precessing net magnetisation. This depends on the B_0 fields in two ways. First, the net magnetisation of the sample depends linearly on B_0:

$$M_0 = N\gamma^2\hbar^2 B_0/4k_B T,$$

where N is the amount of spins per unit volume, γ is the gyromagnetic ratio and T is temperature.

Second, the amplitude of EMF $\mathcal{E}$ induced in our receiving coil depends on the rate of flux change. The frequency of precession influences this rate, and lowering the B_0 field lowers this Lamor frequency. From Hoult and Richards [25], we learn that:

$$\mathcal{E} = \frac{d}{dt}(\mathbf{B_1} \cdot \mathbf{m}) = \omega_0 B_1 V_s M_0, \quad \omega_0 = \gamma B_0,$$

where $\mathbf{B_1}$ is the coil magnetic field per unit current and $\mathbf{m}$ is the total magnetisation.

Combining the above two equations, we find the largest challenge of low-field MRI summarised in an equation:

$$\mathcal{E} \propto B_0^2,$$

the signal strength decreases quadratically with the B_0 magnetic field. Moving down to 59 mT from a conventional 1.5 T scanner means we lose a factor of 625 in signal strength.

However, this does not mean all is lost. Using the above equations, we can estimate our expected signal-to-noise ratio to see if there may be something left to salvage. Using the analysis described in [25], we will calculate SNR $= \mathcal{E}/V_N$, where V_N is the root-mean-square (RMS) voltage of the noise.

We first find the signal by filling in the above equations. As sample material, we use oil, in which the mass fraction of hydrogen is approximately 2/12, having two hydrogen atoms for every carbon atom, and we estimate density to be 1g/cm^3. We estimate our volume to be 1 cm^3, which would be a decent voxel size for first experiments. Our resonance frequency is approximately 2.5 MHz. Finally, we need to estimate B_1. For this we use the infinite solenoid approximation, $B/I = \mu_0 n$, where n is the winding density, which we choose to be 1 cm^{-1}, corresponding to our experimental realisations that are described later. Altogether, we find:

$$\mathcal{E} = 0.57\ \mu V.$$

Our main source of noise will be Nyquist-Johnson noise [24, 25]. Nyquist noise is a thermal white noise that originates from the coils resistance. Both coil wiring losses and lumped element losses contribute. RMS voltage is given by [25]:

$$V_N = \sqrt{4 k_B T \Delta f R},$$

where R is the resistance and Δf the bandwidth of the coil. In our case, this is around 20 kHz.

Internal resistance is estimated using simple RLC-circuit equations. The Q-factor of such a circuit can be expressed as: $Q = 1/R\sqrt{\frac{L}{C}}$. Because our inductor is hand-wound, we do not know its inductance, but because we do know the resonance frequency $\omega_0 = 1/\sqrt{LC}$, we can substitute it. After rearranging, we recover an equation for the resistance: $R = \frac{1}{RC\omega_0}$. We insert typical numbers for our coils: $C = 1$ nF, $Q = 120$, $\omega_0 = 2\pi \cdot 2.5$ MHz (more details in the materials section), and find:

$$R \approx 0.5\ \Omega$$

With these numbers we find for the noise:

$$V_N = 13\ nV,$$

and thus

$$\text{SNR} \approx 44.$$

This figure tells us that in a perfect setup with 0.5 Ω of loss, our theoretical upper limit from a single cubic centimeter is an SNR of 44. This also tells us that it could be possible to build a low-field scanner with, say, 5 mm resolution, if we build a low-loss setup and include averaging of our measurements to increase SNR.

2.3 Calculating coil B_1 field through Biot-Savart

In this section, we will describe a method for calculating the B_1 field as a function of input voltage of a coil with resonance circuit. This can be useful in coil design, because one can determine in advance whether a coil design can produce the required excitation pulse as well as estimate the sensitvity of receive coils. The only experimental input that is needed, is the Q-factor of the coil and the tuning capacitance used. Through measuring both the Q-factor and the power needed to produce a 90 °flip angle for realised coils, we will later on test the accuracy of this method.

We begin by recalling two equivalent definitions of the Q-factor [26]:

$$Q = 2\omega_0/\Delta\omega^*, \quad Q = 2\pi\frac{\text{stored energy}}{\text{loss per cycle}}$$

Here, ω_0 is the resonance frequency of the coil and $\Delta\omega$ the bandwidth, defined as the frequency between the -3 dB acceptance points.

The first definition allows us to determine the Q factor experimentally using a network analyser. The second definition we will use to calculate the B_1 values from the measured Q-factor. To do this, we will assume that 1) during transmission, power dissipated in the coil is equal to the input power, and 2) At maximum voltage accross the coil, all energy is stored in the tuning capacitor. Declaring V_{in} to be the voltage of input power, V_{max} to be the voltage inside the resonator, C the tuning capacitance and Z the coil total impedance (matched to 50 Ω), we can write:

$$Q = \omega_0\frac{CV_{max}^2}{V_{in}^2/Z}$$

and after rewriting:

$$V_{max} = \sqrt{\frac{QV_{in}^2}{\omega_0 CZ}}$$

*p.508 of reference

Next, we will calculate the current flow through the coil. Let q_0 be the maximum charge stored in the capacitor and assume all current leaving the capacitor flows through the coil. We can write the current through the coil as:

$$I(t) = \frac{d}{dt} q_0 \sin(\omega_0 t)$$

We can find the maximum charge through the maximum voltage:

$$q_0 = CV_{max}$$

and the current amplitude:

$$I_0 = \omega_0 CV_{max}$$

At this point, we need to know the coil geometry to calculate the B_1/I using Biot-Savart's law. For common geometries, the equations are often known and of simple form. For a solenoid, for example, the field in the centre is [26]:

$$B_{1,x} = \int_0^{L/2} \frac{I\mu_0 a^2}{(z^2 + a^2)^{3/2}} dz,$$

where L is the coil length and a is the coil radius. For the centre of a saddle coil, we have [26]:

$$B_{1,y} = \frac{2I\mu_0}{\pi} \frac{l}{d\sqrt{l^2 + d^2}} \left(1 + \frac{d^2}{d^2 + l^2}\right),$$

where d is the cylinder diameter and l is the cylinder height.

Finally, we want to relate the calculated value to measured fields. We do this through finding the 90 degree flip angle as a function of input voltage and pulse duration. An often quoted formula for this is[†]:

$$\alpha = \gamma B_1 t_p,$$

where α is the flip angle and t_p is the pulse duration.

As an excercise, we used a Bloch simulator to test this hypothesis. This simulator is a simple Python interpretation of the script written by Brian Hargreaves from Stanford[‡]. In the simulation, a magnetisation along the z-direction was exposed to a model of our B_1 field and our static B_0 field. We measured how much time it would take before a 90 °flip was obtained. These results are plotted in figure 2.1.

[†] p. 212 of [27]

[‡] `http://mrsrl.stanford.edu/~brian/blochsim/`

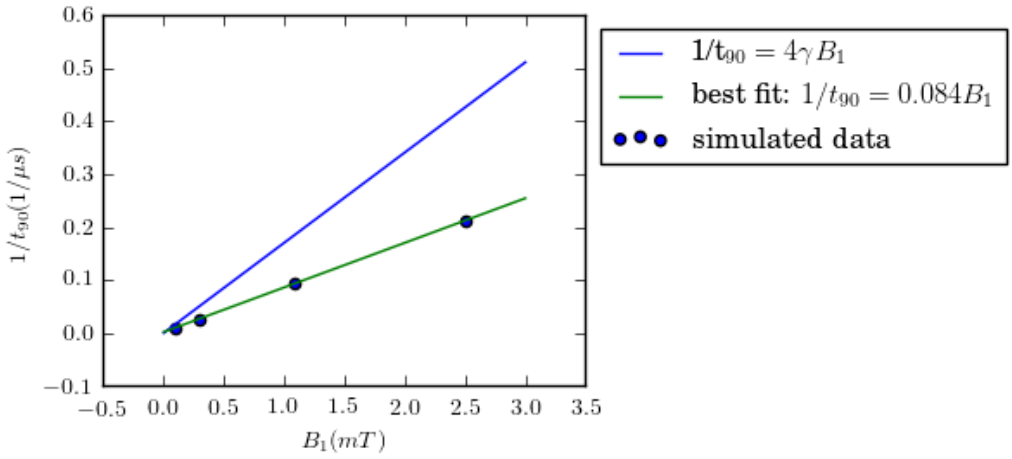

Figure 2.1: *Inverse pulse duration as a function of B_1 field for a 90 degree flip angle. The simulated data (dots) and fit (green) are plotted alongside the standard equation from literature (blue).*

We find a clear linear relation with a coefficient that is almost exactly one half of the predicted value. The reason for this difference was not found, but the fact that it is very close to an integer value leads us to believe there may be a systematic error in our simulation. For this reason, we use the well-established flip angle equation above in future calculations.

Returning to the main goal of this section, the flip angle equation and the B_1-field equation allow us to determine what amplitude and duration are needed for a specific flip angle. It will aid us in coil design and simulation. Conversely, we can compare this to measured flip angles to determine the accuracy of this method, which we will do in the results chapter, section 4.5.

Chapter 3

Materials and methods

A great part of developing the new scanner consists of hardware development. In this section, we will describe the hardware in our current setup.

We will begin by giving an overview of the different components of the setup, which is depicted in figure 3.1. To perform a measurement, a sample is placed inside a permanent magnet Halbach array, which produces the B_0 field. Measurements start and end with a computer. A hardware interface takes the computer's instructions and produces a RF transmission pulse. An amplifier increases the energy in this pulse. The pulse is transmitted by coils inside the magnet array, that surround the sample. Receive coils (which can be the same as the transmitting coils) capture the NMR response of the sample. The weak signal is amplified by a preamplifier. Another hardware interface captures the signal and sends the data back to the computer. Here, the data is processed.

This setup detects NMR signal, but is not yet capable of imaging. To do this, spatial encoding mechanisms need to be implemented. Progress towards this goal is discussed in chapter 5.

In the following sections, we will discuss the individual components of this setup. All components are connected by 50 Ω coax cables.

3.1 Coil designs

RF Coils are at the heart of the scanner. There are several important properties that define a coil, such as geometry, resistance and number of windings.

The amount of electromotive force (EMF) that a precessing net magnetisation can induce in a coil, depends linearly on the magnetic field per

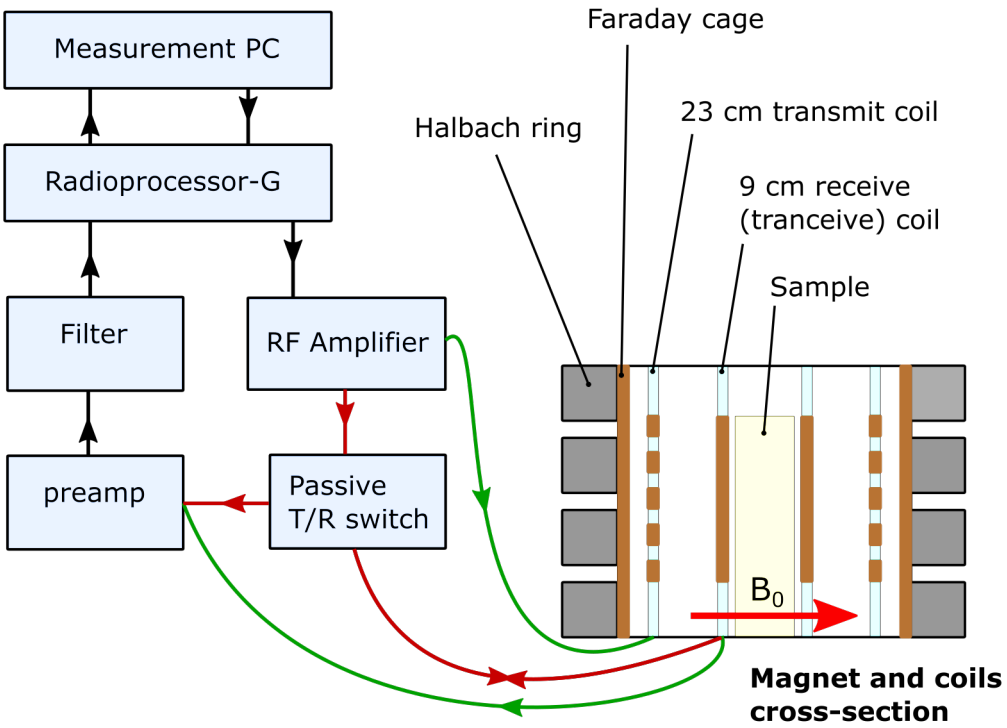

Figure 3.1: *A schematic of the setup used in experiments. Lines with arrows show the control flow through the setup. The green and red lines demonstrate two different modes of operation: when the green lines are connected, we use separate coils for transmit and receive, whilst the red lines show the transceive setup.*

unit current that can be produced by the coil [25]. In general, the field per unit current increases with the winding density of the coil. In this regard, more windings are better. On the other hand, more windings also increase the amount of resistance in a coil, increasing losses and consequently lowering the Q factor. In the case of a receive coil, this means a lower sensitivity. Additionally, capacitance between the windings increases, giving the coil a self resonance that will eventually make capacitive tuning impossible. Altogether, the question: 'what is the optimal amount of windings?', does not have a straightforward answer.

There are two coil geometries that we will consider in this thesis: solenoid and saddle coils. First, we will use a single solenoid for both transmit and receive using a passive switch. Transmitting and receiving using the same coil will be called *tranceive* to avoid confusion. After that, we will test two pairs of coils: first, a saddle receive coil and a solenoid transmit coil, fol-

lowed by the inverse, a saddle transmit coil and a solenoid receive coil.

All of our coils are tuned and matched capacitively and symmetrically. Figure 3.2 shows the circuit used to tune. The two matching capacitors C_m have the same value and are used to change impedance to 50 Ω.

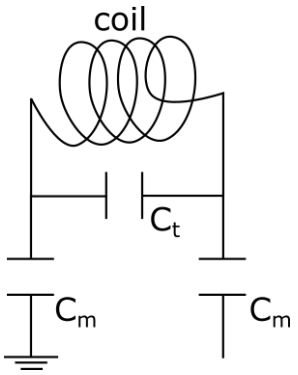

Figure 3.2: *The electrical circuit used to tune our coil to the right frequency and to match it to* 50 Ω

The solenoid coil that is used for tranceive is wound around a 9 cm diameter PPMA cylinder. It has 10 windings and is 10 cm high. It is tuned using $C_t = 663$ pF and $C_m = 136$ pF. A second receive coil, a saddle coil, was also constructed on a 9 cm cylinder using $C_t = 240$ pF and $C_m = 95$ pF. This coil has 5 windings in both loops and is also 10 cm high. Both receive coils were matched with low-loss capacitors, resulting in a high Q and small bandwidth, which is 18 kHz for the solenoid en 22 kHz for the saddle coil.

Two transmit coils were made on 23 cm diameter cylinders. The saddle coil ($C_m = 121$ pF, $C_t = 380$ pF) has three windings in each loop, where the solenoid ($C_m = 470$ pF, $C_t = 1050$ pF) has seven windings in total. Both coils were matched and tuned using capacitors that have more loss than necessary. Introducing additional loss increases the coil bandwidth, meaning the coil can excite over a larger (> 100 kHz) bandwidth. However, in practice, the long pulse duration needed to obtain a 90°or 180°flip, which is on the order of hundreds of microseconds, limited the excitation bandwidth to a few kilohertz. Figure 3.3 shows images of the two pairs of transmit and receive coils.

In two-coil experiments, the larger transmit and smaller receive coil are placed concentrically in the Faraday cage. Coupling between the two is minimised by using designs that, to large extent, create magnetic fields that are orthogonal to each other. In practice however, coupling can be as high as -14 dB and is dependent on the relative orientation. By rotating

the receive coil with respect to the transmit coil, coupling is ensured to be -40 dB or lower. The receive coil diameter was chosen to be smaller than the transmit coil, because for comparable diameters we were not able to reach sufficient decoupling yet. Additionally, this also means the receive coil becomes more sensitive.

3.2 Tranceive using a passive switch

When using the same coil to both transmit and receive, a switch is needed. During transmission, the high power RF from the amplifier needs to enter the coil, while the sensitive readout equipment is shielded. Milliseconds after, however, the signal detected by the coil needs to reach the readout equipment with high efficiency. Both passive and active switches exist. Here, we will work with a passive switch that is based on crossed diodes, based on the proposition by Bendall *et al.* [28].

The schematic of the design is shown in figure 3.4. We used values of $L_1 = 2.8\ nH$, $L_2 = 5.6\ nH$, $C_1 = 1\ nF$ and $C_2 = 4.7\ nF$.

The idea of the design is the following. Consider only the part between the left two pairs of crossed diodes. At high voltage, when the RF amplifier is on, the crossed diodes act as shorts. The π-network between the two pairs acts as a quarter-wavelength transformer and transforms the short to an open. This makes sure that little power enters the π-network, and most power flows from the amplifier to the coil.

When the small receive voltage in the coil is present, the diodes act as high resistances. Power can flow from the coil to the preamp, passing through a low-pass and high-pass filter along the way, which are tuned to have a transmission at 2.5 MHz. The circuit between the right two pairs of crossed diodes is simply a second stage that makes the insulation of the switch better.

We have measured the switch's properties for both transmission and receiving. For the transmission measurements, we connected the RF amplifier to the switch, sending an approximately 60 V_{pp} RF signal at 2.5 MHz. Figure 3.4 shows three different measurements. First, we measured the RF amplifier voltage V_{RF} over a 50 Ω load after 40 dB of damping. Next, we connected the switch and measured the probe output V_{probe} with the same damping, while the preamp output was connected to a load. Finally, we measured the preamp output V_{out} while the probe was connected to a load.

We see that almost all power from the RF input is sent to the probe. The preamp output is limited to about 2 V_{pp}, which we found to stay con-

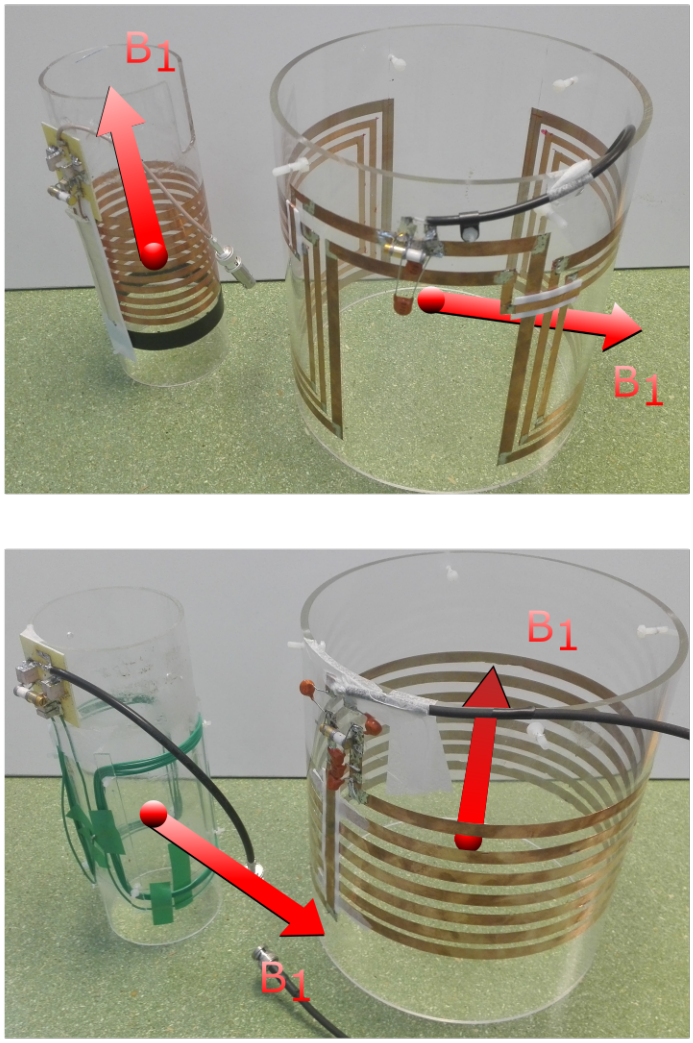

Figure 3.3: *The coils used in the experiments. Top: On the left, the 9 cm diameter solenoid used for both tranceive and receive. On the right, the 23 cm saddle transmit coil. Bottom: On the left, the 9 cm saddle receive coil. On the right, the 23 cm solenoid transmit coil. The arrows in red indicate the direction of the B_1-fields in the centres of the coils.*

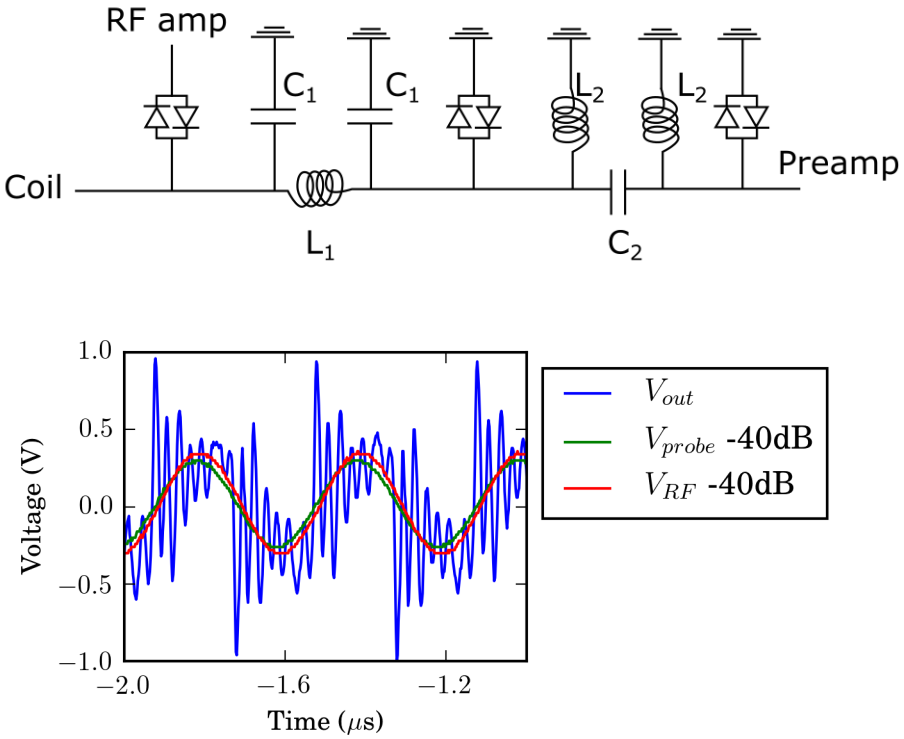

Figure 3.4: *The passive switch.* ***Top****: The schematic of the passive switch used in tranceive operation.* ***Bottom****: An example of the passive switch's transmission properties. The red trace displays input RF after 40 dB of damping. The green trace shows the RF voltage that reaches the probe, measured with the same damping. The blue data shows the protected preamp output.*

stant with increasing RF input voltage. The preamp output waveform is different from the input because of the non-linear behaviour of the diodes.

Finally, we tested the switch's receive properties by connecting a waveform generator to the probe input. We connected a load to the RF input and measured the preamp output. We found $\frac{V_{out}^2}{V_{probe}^2} = \frac{(9.1\ mV)^2}{(10.7\ mV)^2} = 72\%$ transmission at low voltage.

3.3 The Halbach magnet array

Our B_0 field is produced by a Halbach permanent magnet array. These arrays, named after their inventor Klaus Halbach [29], are specific arrangements of permanent magnets that have high magnetic field on one side of

the array while minimising field on the other side.

In our case, we use a circular array (see right figure 3.5), which means that we have a high field inside the ring that points in a single direction everywhere, while we maintain a low field outside. Halbach arrays are characterised by an integer, and we use the $k = 1$ configuration, corresponding to a dipole field inside the magnet. We use 24 cubic NdFeB N52 magnets to approximate a continuously changing magnetisation orientation. The magnets have vertices of one inch. Similar designs have been studied extensively previously, see for example [30]. The resulting magnetic field points in the plane of the ring, which we define to be the z-axis. We combine four circular arrays into a cylinder to produce a magnetic field that is also homogeneous in the x-direction. The height of the four stacked rings with interspacing is 18 cm. The magnet array produced by the TU Delft, where it was designed by Lennart Middelplaats.

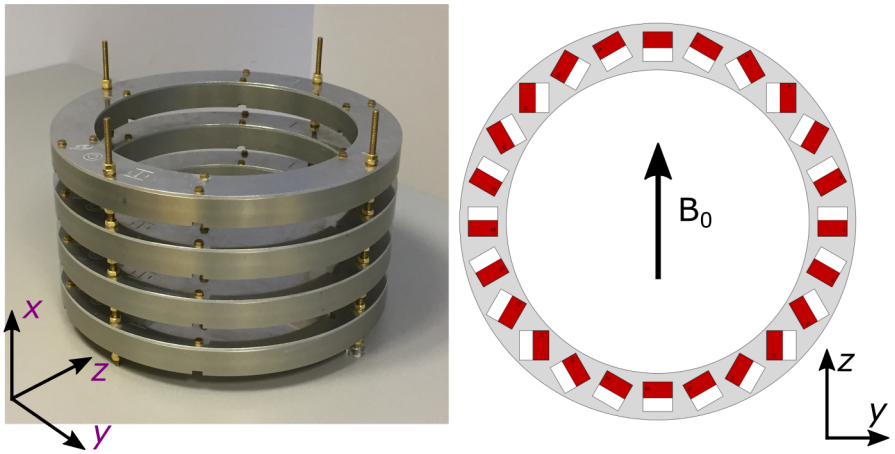

Figure 3.5: *The Halbach magnet array used in our experiments. Left: a picture of the array, consisting of the stacked rings of magnets. Right: a schematic showing the distribution of cubic magnets in a single ring. The inner diameter of the ring is 26 cm.*

The resulting magnetic field has been measured using a Hall probe. In figure 3.6, we show three different slices that pass through the centre of the magnet. Only positive values of the z-axis were sampled and this data was mirrored to estimate field for negative z-values. The top two figures show that the magnetic field decreases when moving away from the centre in the x-direction (along the bore), but increases in the other two directions. The bottom figure shows the centre slice orthogonal to the magnet bore. Here, the magnetic field is lowest in the centre and increases towards the edges. It increases more rapidly along the z-axis than along the y-axis. The

field in the centre has a magnitude of 58.64 mT, corresponding to a Lamor frequency of 2.497 MHz. Within a 20 by 12 cm FOV, we have a frequency variation of 330 kHz, and in a 10 by 4 cm FOV, 80 kHz.

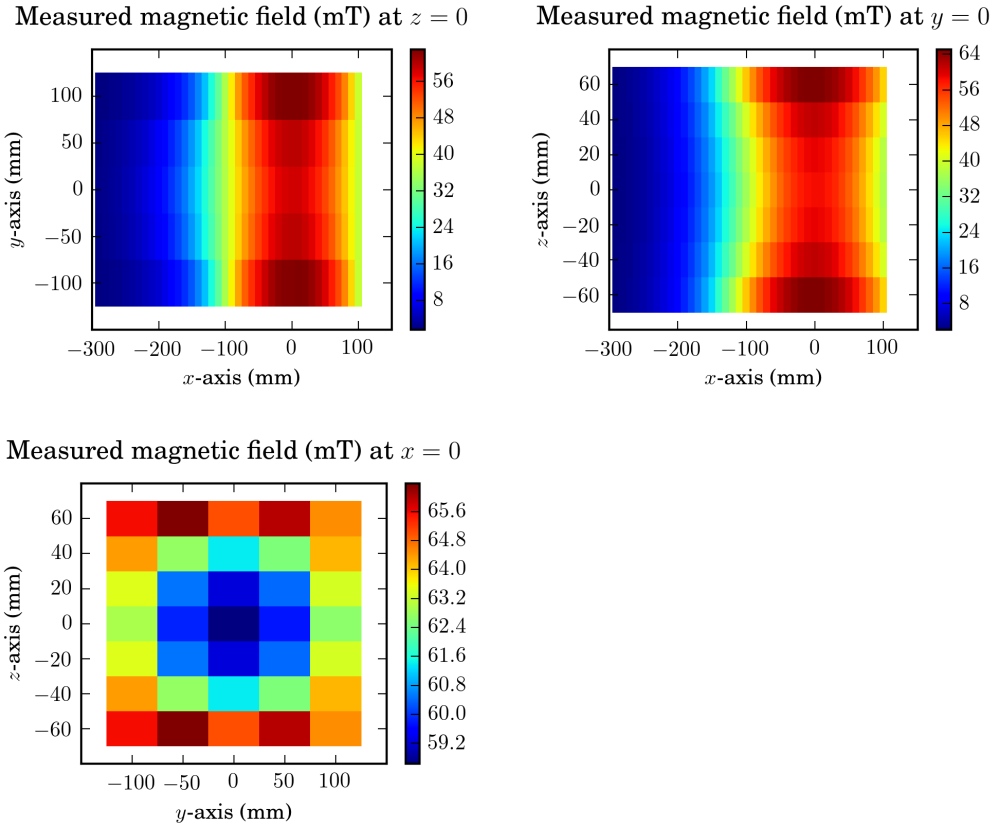

Figure 3.6: *Magnetic field magnitude maps of three orthogonal slices through the centre of our magnet. The top two figures show rapid decay along the bore (x-axis) of our magnet, whilst the bottom figure shows the well-shape of the field strength in the zy-plane.*

3.4 The Faraday cage

A Faraday cage surrounding the coil is essential, because it prevents the unwanted pick-up of noise. For the efficiency of a Faraday cage, it is important that it is at least several skin depths thick. Using the properties of copper, we can calculate* that the skin depth at 2.5 MHz is 41.2 μm.

*See, for example, p.414 of [31].

We built a cylindrical Farday cage that fits inside the magnet bore. By using 0.3 mm thick copper, we satisfied the skin depth condition. The cage was finished off with a top and bottom lid, in which we installed barrel connectors to connect the coil coax to the outside. Making electronic connection between the shields of these cables and the Faraday cage turned out to be essential for the cage to work.

3.5 The analogue-to-digital interface

The interface between the measurement computer and the RF signals is a Radioprocessor-G PCI board by SpinCore Technologies[†]. This board produces the RF pulses that are required for the different protocols (Gradient echo, Spin Echo and CPMG). During the measurements described here, we restricted ourselves to hard pulses with a block-shaped envelope, corresponding to sinc-shaped distributions in the frequency domain. The left plot in figure 3.7 shows an example pulse shape for a very short pulse. The right plot shows the sinc-shaped frequency profile and limited bandwidth of a more realistic, longer pulse.

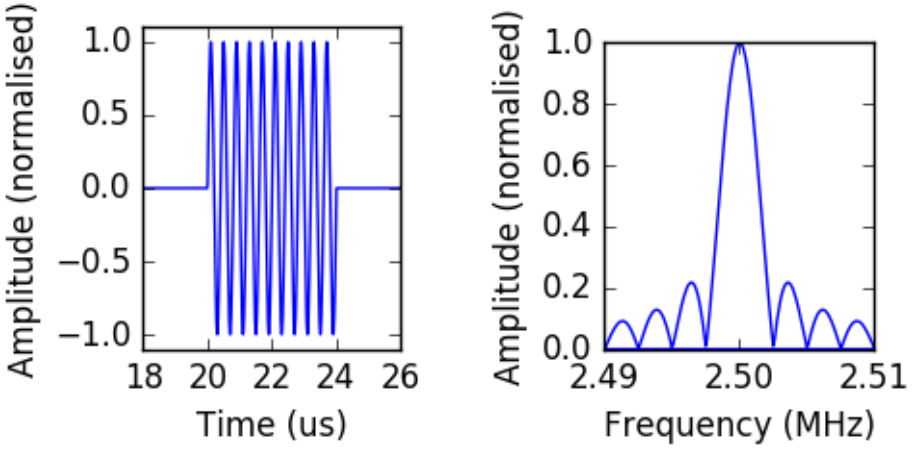

Figure 3.7: *RF hard pulses are used in our experiments. The left figure shows a short (4 µs) hard pulse at 2.5 MHz in the time domain. In reality, the pulses we use have a length on the order or hundreds of microseconds. The right figure shows the spectrum of a 400 µs typical pulse, which has a bandwidth of only several kHz.*

[†] `http://www.spincore.com/products/RadioProcessor-G/RadioProcessor-G.shtml`

Additionally, the Radioprocessor-G records the received signal. This is done by demodulating the measured voltage by exactly the excitation frequency, leaving a low-frequency signal that is output digitally to the measurement pc.

3.6 Amplifiers

We use a custom made amplifier to amplify the low power RF excitation pulses of the Radioprocessor. The amplifier was built by Danny de Gans at the TU Delft. The amplifier has a maximum output of 1 kW, or 894 V_{pp}. It has an amplification of about 50 dB.

Between the passive switch and the Radioprocessor-G, the small signal is amplified by a Miteq AU-1054 30 dB preamplifier.

Chapter 4

Magnetic resonance measurements

In this chapter, we report on the first measurements of magnetic resonance performed with our setup. For these measurements, the spin echo in single form (90°,180°pulse) and in pulse train form (CPMG) (90°,180°,180°, etc.) were used. It is not possible with our current setup to measure free induction decays (FIDs). The reason for this is that the short FID overlaps with the ringdown of our transmit coil, which masks the FID even in the case of separate transmit and receive coils. Ringdown time can be lowered by active switching mechanisms inside the coils, but during this research, we avoided this problem by restricting ourselves to spin echoes.

4.1 Spin echoes in tranceive mode

First, we will describe measurements performed using the tranceive setup. The sample for these measurements is a large bottle of sunflower oil that fills up almost the entire coil volume. The 1 liter bottle has a diameter of 75 mm and a height of 260 mm. Excitation is performed at 2.50 MHz with pulse durations of 100 and 200 μs for the 90°and 180°pulse, respectively. For each measurement, 100 averages were taken.

To determine the flip angle, we performed an amplitude sweep. The results can be seen in figure 4.1a. The y-axis shows the area under the echo, determined as a measure of the signal strength. The figure contains three peaks, which we believe to correspond to 90°/180°, 270°/540°and 450°/900°flip angles. The peaks are found at amplitudes of 0.05, 0.14 and 0.24 which, assuming a linear relation between amplitude and flip angle, support this hypothesis.

To quantify the clarity of measured echoes, we use the signal-to-noise

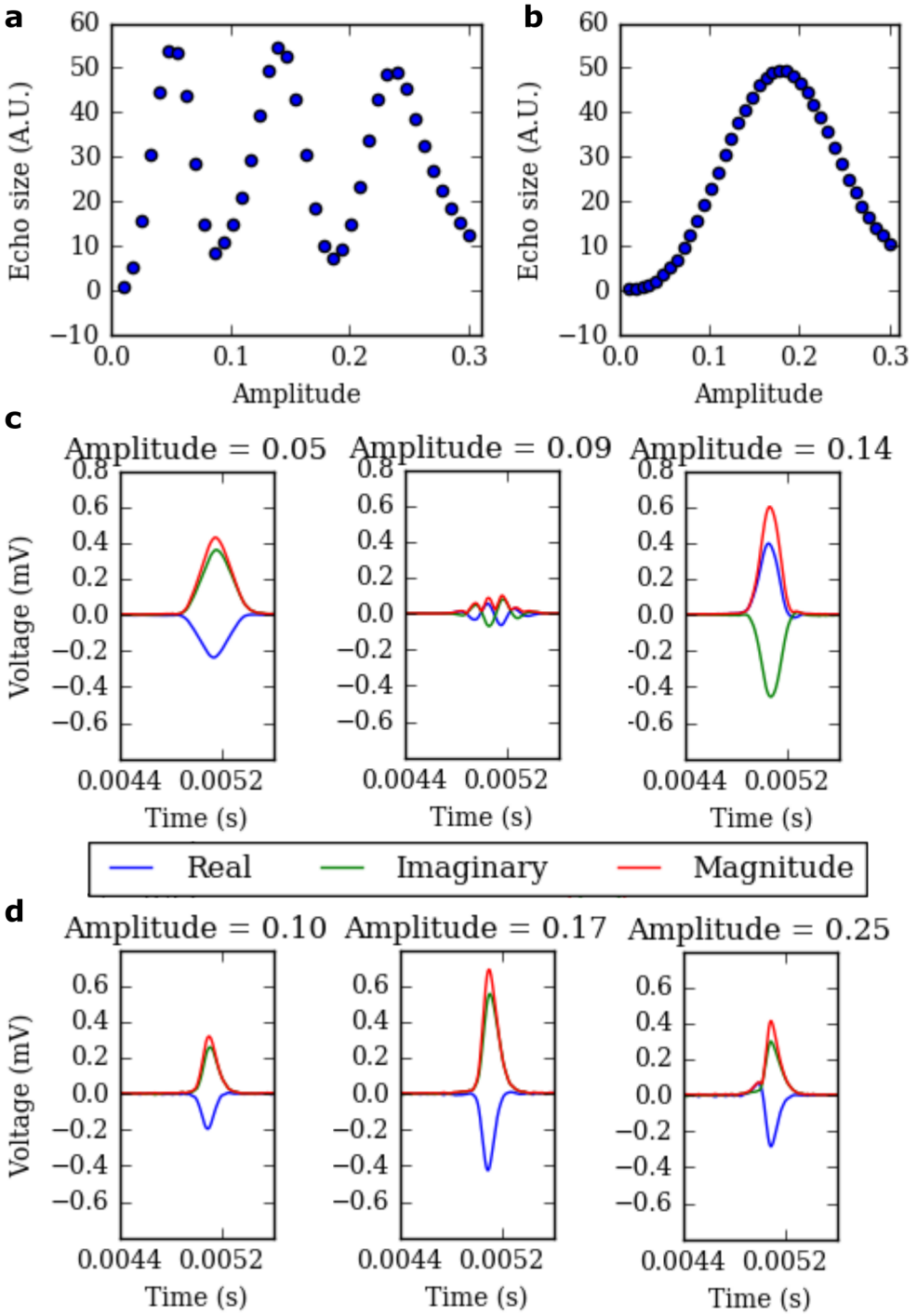

Figure 4.1: *Spin echoes with a solenoid tranceive coil.* ***a*** *Shows an amplitude sweep for a 100/200 µs pulse length.* ***b*** *Shows the same sweep for a 25/100 µs pulse length.* ***c*** *contains four example echoes taken from the sweep of figure a at different amplitudes.* ***b*** *Shows three echoes taken from the sweep in figure b.*

ratio (SNR). To determine SNR, we calculate the area under the absolute signal of the echo, divided by the area under an echo-free part of the same duration, taken from the same signal. For the tranceive mode, the highest SNR reached is 210. To obtain this, we used 100 averages, meaning we would expect an SNR of 21 for a single measurement.

Figure 4.1c shows three echoes taken using the 100/200 μs pulses for different amplitudes, corresponding to flip angles between 90 and 270 degrees. We see that the signal first reduces in strength and then rises again as we increase flip angle. Note that the phase of the echo at 0.14 amplitude has a 180 degree phase shift with respect to the echo at 0.05 amplitude. This can be explained in the following way. Consider the magnetisation right after the excitation pulse, which is located in the xy-plane in both cases. Applying further RF excitation would move the magnetisation in the 270 degree case towards the positive z-axis, whilst for the 90 degree case, magnetisation would move towards the negative z-axis. This can only be possible when the two magnetisations are exactly out of phase with respect to each other. In the figure, we can also see oscillations within the echo envelope at intermediate flip angles. These are caused by the bandwidth of our excitation pulse. The mixing of slightly different frequencies causes these oscillations.

Next, in figure 4.1b, we show an amplitude sweep of the same range, now with a 25/50 μs pulse and only 10 averages. We see the flip angle is more limited and 90 °flip is now achieved with 0.17 amplitude. If the B_1 response to input voltage were linear, we would expect to see the 90 °peak at 0.2. Thus, this indicates there are slight non-linearities, which might be because of the inhomogeneities in the B_1 field across our sample. Individual echoes of this sweep are shown in figure d, where we see an echo for a flip angle of approximately 50, 90 and 130 degrees. Comparing to the echoes obtained at longer pulse duration, we see the echo at a 90 °flip angle decays faster at shorter pulse duration. This is because pulse duration is inversely proportional to the bandwidth of the pulse. Our short pulse excites a broader spectrum, and the combined echo has a shorter T_2^* time. We also see this in the amount of signal we receive. With only 10 averages, we obtain a maximum SNR of 340, which corresponds to a single-shot SNR of 108. The SNR has increased because we excite a larger volume with the shorter pulse. Further decrease in pulse duration is not expected to give further increase in SNR, because the bandwidth of our coil now becomes a limiting factor.

4.2 Measurements with separate receive and transmit coils

Using a separate coil for transmit and receive offers some advantages over using a single coil. First, it allows us to tune the properties, such as bandwidth and geometry, separately. This is advantageous, since transmit coils often have different requirements from receive coils. Also, it omits the need for a switch. Here, we compare the two-channel setups described in the materials chapter to the tranceive setup.

The amplitude sweeps for the saddle transmit and the solenoid transmit are displayed in figure 4.2a and b, respectively. Measurements were performed at 2.5 MHz using a 400/800 μs pulse and 100 averages. The saddle transmit requires a higher input amplitude to reach a 90 $^\circ$flip angle of 0.77, as compared to 0.29 for the solenoid transmit. This is in good agreement with the factor of 3 difference in field per unit current found by Hoult and Richards [25]. Correspondingly, the signal received by the saddle is a factor of 2 lower than the signal received by the solenoid. SNR for the solenoid receive is at most 25, while SNR for the saddle receive peaks at 21.

The echoes in figure 4.2c and d are much longer than those obtained with the tranceive setup. The main reason is that, for the tranceive setup, a much shorter pulse was used. The longer pulse for the two-coil setup has a narrower bandwidth, which corresponds to a longer T_2^* time.

We summarise the comparison between our tranceive and two-coil setups. First, measured SNR for the tranceive setup is much higher. We believe this is mainly due to the larger bandwidth of the shorter pulses that could be used with the smaller tranceive coil. The disadvantage of this is the much shorter echo duration at shorter pulses. Using a large diameter transmit coil has the advantage of a homogeneous field, allowing excitation of a larger volume. However, the long pulse length needed for these, because of our limited amplifier power of 1 kW, removes this advantage. Although, in theory, there clearly is merit to using separate transmission and receive coils, we have not yet been able to demonstrate these in our current setup.

Finally, we want to mention that interesting information can be found in the complex phase of the echo and how this evolves as a function of amplitude. It is easy to see, when comparing figure 4.1 to figure 4.2 that the phase behaves differently. This phase may contain information on the coil's properties. We decided not to analyse the phase data in this thesis, but doing so could be a next step in this research.

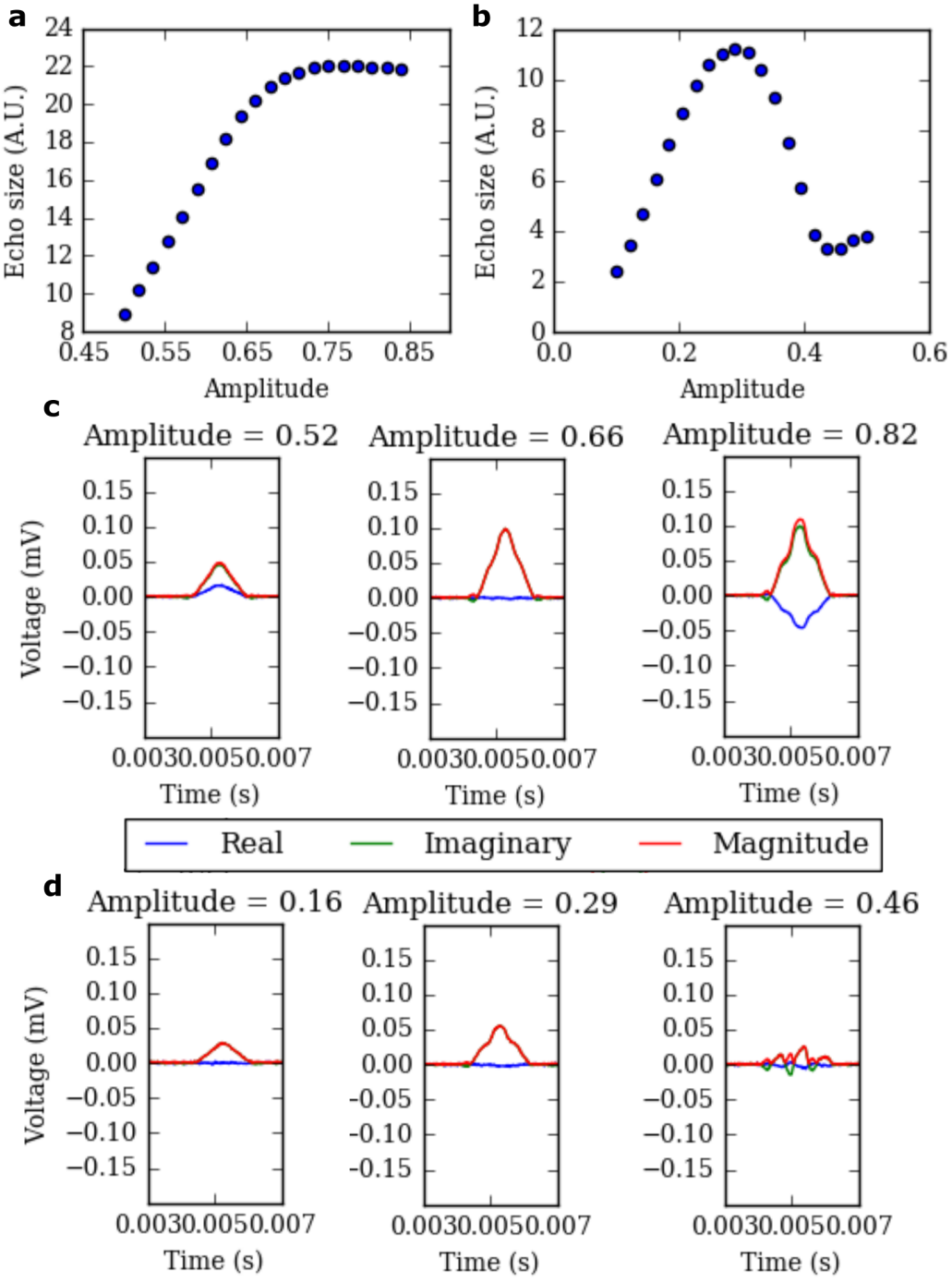

Figure 4.2: *Spin echoes with separate transmit and receive coils.* ***a*** *shows an amplitude sweep with a saddle transmit coil and solenoid receive.* ***b*** *shows an amplitude sweep with a solenoid transmit coil and a saddle receive coil.* ***c*** *displays three example echoes from the sweep in figure a and* ***d*** *shows three echoes from the sweep in figure b.*

4.3 Spin echo pulse trains

A extention of the spin echo is the CPMG sequence [32, 33]. The CPMG sequence consists of a 90 °pulse, followed by a series of 180 °pulses separated by twice the echo time. Between each pair of 180 °pulses, an echo is measured. The echoes decay in time almost solely due to T_2 effects, because T_1 and T_2^* effects are canceled out. Additionally, the sequence can be made more robust to deviation from a 180 °flip by introducing a 90 °phase shift between the excitation and the refocussing pulses. All in all, performing a CPMG sequence measurement and performing an exponential fit to the decay of echo intensity allows one to determine the T_2 time constant.

For these experiments, we used 400/800 μs pulses, an echo time of 5 ms and 100 averages. We acquired 32 echoes, corresponding to a total measurement time of 320 ms. The measurement sampling rate is 100 kHz, i.e. we collect one data point every 10 μs. We performed these tests using the saddle transmit and solenoid receive setup on a large phantom filled with either sunflower oil or water. The results are displayed in figure 4.3.

Subfigure a and b show the first 8 echoes for the water and the oil phantom, respectively. Note that the time axis does not correspond to real time here: data from different echoes is combined in sequence without the appropriate time spacing. This is corrected for later, before fitting the decay rate. The shape of the echoes changes through time, indicating that different frequencies undergo the sequence in different ways. Note also that the water gives a much weaker signal than the oil. Figure c shows the decay of echo amplitude for water. Using an exponential fit, we determine the T_2 time to be about 240 ms. Figure d shows these results for oil, where we find T_2 = 91 ms. For both samples, the first two echoes appear to be outliers from the exponential decay, as can be seen in figure c and d, but also in figure a and b.

4.4 Noise measurements

To determine the amount of noise in our setup and the degree at which different components contribute, we performed noise measurements. To do this, we ran the spin echo programme, but with the amplifier unblanking signal disconnected. Thus, the amplifier can be connected to our coil for noise considerations, but will not amplify the incoming RF pulses. We measured a 28 kHz bandwidth, cut off by a digital filter. For several different combinations of hardware attached, we determined the root-mean-square voltage of the noisy signal in 100 single-shots and determined the

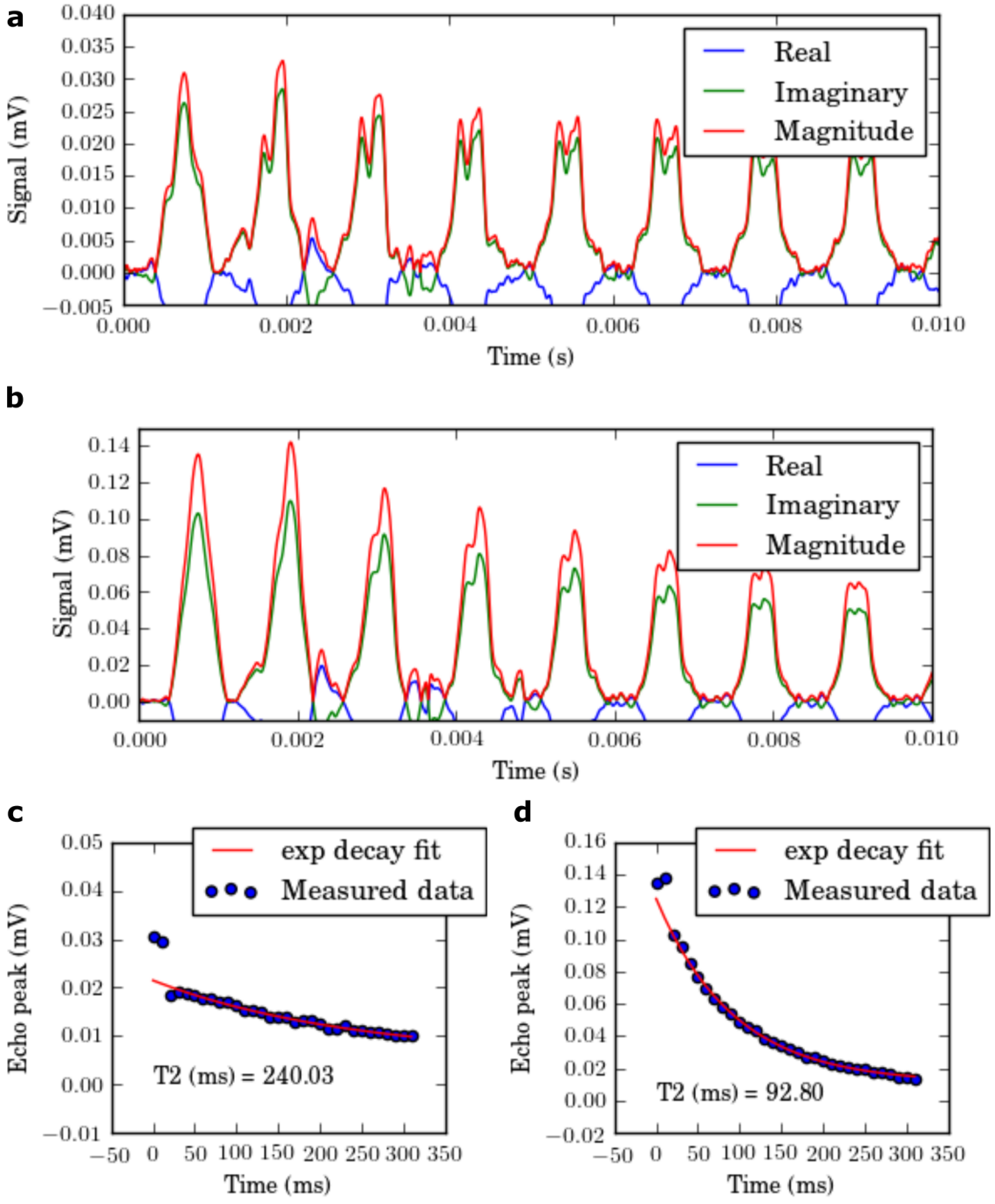

Figure 4.3: *Results of CPMG experiments on water and oil phantoms.* ***a*** *Shows the first 8 echoes measured for the water phantom.* ***b*** *Shows the same measurement for the oil phantom.* ***c*** *Displays the decay of the echo amplitude as a function of real time and the exponential decay fit.* ***d*** *Shows the same for the oil phantom.*

Setup	$V_{rms}(\mu V)$
No cable connected to Radioprocessor card (baseline)	8.0 (0.7)
Preamp connected, but its input not connected to coil	9.4 (0.6)
Saddle receive coil connected through preamp	11.5 (0.9)
Solenoid transmit connected through preamp	9.0 (0.6)
Saddle coil, preamp, Faraday cage without lid	52 (4)
Saddle coil. preamp, no Farday cage	565 (30)

Figure 4.4: *Noise levels measured with different parts of the setup connected. The levels are given as an average root-mean-square voltage of the noise. The number in brackets is the standard deviation within the set of measured values.*

average value and standard deviation within the set. The results are displayed in figure 4.4.

First, we see that adding an active preamp, with an open input, to the Radioprocessor card gives an increase in noise. This noise is, however relatively small compared to the already present noise level in the card itself. Connecting a coil to this gives a further increase in noise level for the high-Q receive coil, but not so much for the low-Q transmit coil. The low-Q coil has a higher resistance because of the components that were chosen and is thus expected to give more Nyquist noise than the high-Q coil. These results suggest the noise may actually come from RF pickup up by the coil, in which case the high-Q coil is expected to show a higher noise level.

The V_{rms} generated by the coil can be estimated by substracting the internal noise of the Radioprocessor card and the preamp. We find $V_{rms,coil} = \sqrt{11.5^2 - 9.4^2} = 6.6\mu V$. Note that this is after preamp amplification. To estimate coil noise, we remove the amplification and find:

$$V_{rms,coil} = 10^{-30dB/20dB} \cdot 6.6\ \mu V = 209\ nV$$

By measuring coil wire resistance and using lumped element specifics, we determine the maximum dissipative resistance to be 5 Ω. Thus, the Nyquist noise is expected to be 48 nV. This suggests some reduction in noise can still be obtained. For the the transmit coil, this is not immediately clear. The results suggest the preamp may produce more noise when the input is left open and therefore it is difficult to separate the smaller contribution of the coil noise. The above estimate thus serves more as an upper bound.

Finally, we turn our attention to the Faraday cage. The noise figure without cage shows its crucial role in our setup. However, the indication

Setup	Measured B_1 (μT)	Theoretical B_1 (μT)
Tranceive 25/50 μs	59	319
Tranceive 100/200 μs	235	1090
Saddle transmit 400/800 μs	29	189
Solenoid transmit 400/800 μs	29	432

Figure 4.5: *A summary of the measured B_1 values and the estimated values for four different experiments.*

that noise may be due to coil pickup is a hint that it may not shield well enough. A measurement without lid was performed to show that the cage still maintains some of its functioning in this case. This is an interesting lead, since in the final design, the Faraday cage will have to be altered to allow a patient inside the scanner. One idea would be to use an open-ended cage. Such a cage, when it is sufficiently long, could act as a waveguide that, for the diameter we use, can not support a mode of 2.5 MHz radiation. These results show, however, that for this effect to be strong enough to be useful, the cage will have to be made longer.

4.5 Comparing measured B_1 to theory

Using our amplitude sweeps, we can now determine whether our coils behaved according to the model described in section 2.3. To do this, we gather the Q factor, as determined using a network analyser, the tuning capacitance needed and the amplitude and pulse duration needed for a 90°flip. From this last variable, we can calculate the B_1 amplitude, which will be the experimentally determined value. From the other factors, we can predict the B_1 field we expect by using our model. The results of these calculations can be found in figure 4.5.

Our model is cleary overestimating the strength of the B_1 field. For the tranceive setup and the saddle transmit, the esimation is a factor of 5-6 too high, while for the solenoid transmit coil, the factor is as high as 15. We are overestimating the current that flows through the coil, since the field per unit current is not likely to be wrong by such a large factor, since it is based on Maxwell's well-established laws. Thus, our model for the current flow calculation is incorrect. It may well be that we are underestimating losses and thus overestimating the voltage that builds up inside the resonant circuit.

Chapter 5

Developing 2D imaging with rSEMs

After having performed basic NMR signal acquisition, we now look towards the next milestone in the portable scanner project: 2D imaging. In this chapter, we will describe the encoding technique of rotating spatial encoding magnetic fields (rSEM), which we want to use for this imaging. After that, we will discuss simulations that we performed to test whether the encoding method is feasible in our system.

5.1 rSEM encoding

To produce a 2D image, one needs to vary two parameters during the MRI scan. In gradient field encoding, these two parameters would be the strength of the phase gradient and the time of readout of a data sample during the frequency-enconding gradient. For rSEM encoding, the first is replaced by the rotation angle of the rSEM. The second parameter is still the time of readout, but now no gradient fields are switched on or off rapidly between excitation and readout. There is just one field, the rSEM, that does not vary during excitation. This less common concept is actually based on one of the very first papers on MRI [34], and a variation was later proposed as way to reduce gradient coil noise [35]. The adaptation that we will describe and study here is the one used by Cooley *et al.* [10], which is designed to use the already present inhomogeneity of the B_0 field as the rSEM, removing the need for additional encoding fields and contributing to the portability of the design. A measurement consist of time-domain samples of a spin echo from the entire field of view (FOV) for each rota-

tion of the rSEM. Rotations can, for example, be chosen to be steps of 2 degrees within the range of one full revolution. From this data set, one can then reconstruct the image. A schematic of a rSEM scan is shown in figure 5.1a

To explain how the reconstruction works, we first write the measured signal as a function of the image and measurable parameters [10]:

$$S_r(t) = \sum_x C(\mathbf{x}) e^{i2\pi k(r,\mathbf{x},t)} m(\mathbf{x})$$

or, in matrix form:

$$S_r = E_r m(\mathbf{x})$$

Here, $S_r(t)$ is the measured signal at time t for rotation r. It is calculated by summing over the 2D voxels at positions $\mathbf{x}$, each of which has its own phase evolution $k(r, \mathbf{x}, t)$, that depends on the magnetic field, and thus the rotation and position, and the time. The factor $C(\mathbf{x})$ is the spatially varying complex coil sensitivity. Finally, $m(\mathbf{x})$ is the magnetisation, or the image. This equation shows that we can calculate the signal, if we would know the rSEM values, the coil sensitivity and the image. The reconstruction works by inverting this problem: knowing the signal, the coil sensitvity and the magnetic field, can be reconstruct what the image has to be?

To solve this question the Algebraic Reconstruction Technique, based on an idea originally intended for CT scans [36], is used. This technique involves iterating over the different measurement points. For each data point with a specific time and rotation, the magnetisation is updated. After iterating through all data points several times, the magnetisation converges to an image. The exact details are described in the PhD-thesis of Clarissa Cooley [9].

An intuitive way of looking at this method is demonstrated in figures 5.1 b and c. In figure b, we see a heatmap plot of the magnet used by Cooley *et al.* [10], which is qualitatively comparable to ours. Here, we follow two points in the sample, a and b, as we rotate the magnetic field. Figure c shows how the Lamor frequency for these two points changes. Remember now that the time-spaced measurement points also contain the frequency information of the echo. In figure c, we see that the two points have unique frequency contributions to the echo as the magnet changes. It is through this unique 'footprint' of each point, that the contribution of each voxel can be determined.

This explanation immediately brings us to another important consideration. In a magnetic field such as that one in figure 5.1b, not every point has a unique footprint. In particular, two points that are each others mirror image through the centre of rotation, give the same contribution. This

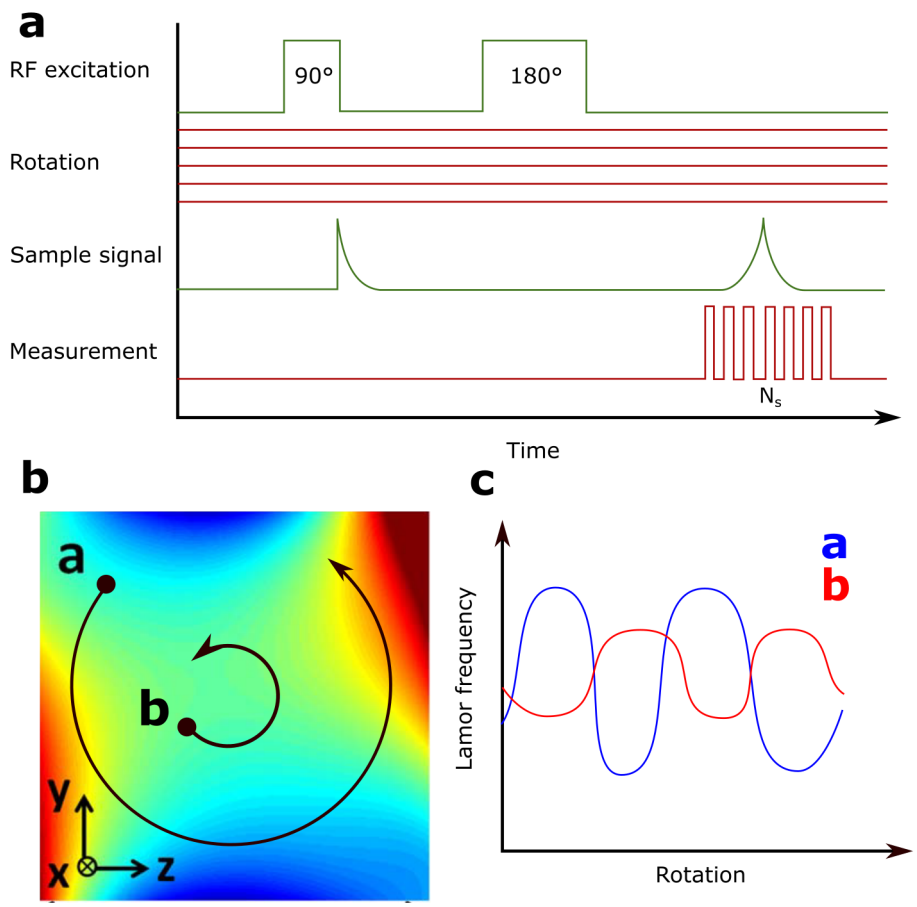

Figure 5.1: *Rotational encoding for 2D imaging.* ***a*** *Shows the pulse sequence of a rSEM measurement, demonstrating no settings are varied during a single excitation.* ***b****) Shows the paths through the magnetic field for two different points during rotation.* ***c****) Shows how the Lamor frequency for these two points varies as a function of rotation angle.*

causes so-called aliasing, greatly reducing image quality. A solution is to perform measurements using multiple receive coils, each having a different sensitivity map. The information from the additional coils can easily be included in the reconstruction method and can then be used to distinguish the voxel at point from its mirror image.

5.2 Simulations

It is our aim to reproduce the results by Cooley *et al.* in our own setup, before moving on the 3D imaging. The first step to do doing is this, is to perform the reconstruction in simulation to both better comprehend the method and to learn whether it can be applied in our magnetic field. To this end, we first use an interpolated map of our magnetic field together with a phantom design to produce a simulated spin echo for different rotations. This data is then fed into the reconstruction method, as you would with measured data, to run the reconstruction algorithm.

Generating the signal happens through the above signal equation. For $m(\mathbf{x})$, we use our phantom and to determine k, we use magnetic field data. Coil sensitivity is set to be uniform. No noise is added to the signal, but it is discretised at a realistic sampling rate of 1 μs^{-1}. Just like with our measurement system, the signal is demodulated by the centre frequency. The FOV is a 10×10 cm square in the centre of our magnet that is described by a 50×50 grid of voxels.

Figure 5.2 shows these results. The letters LUMC in the top left function as our phantom. The next figure shows the echo calculated from this phantom at no additional rotation. This echo, and those at other rotations, are used as input for the reconstruction algorithm. We see that already after half an iteration, the phantom can be recognised. As said before, with uniform coil sensitivity, a voxel can not be distinguished from its mirror opposite. Therefore, the phantom's mirror image also appears. The following 49 iterations make the image more clear and reduce blurring in the centre. However, even after as much as 100 iterations, the blurring in the centre does not completely disappear. This is because our magnetic field has a local minimum in the centre and points close to it have feel only a small change in Lamor frequency during rotation. On a regular laptop, using python code that was not optimised for speed, each iteration takes about 10 seconds.

The simulations indicate that the 2D imaging method may be applicable in our system. However, there are still several hurdles to overcome. First, an infinite coil bandwidth was assumed. In reality, the bandwidth

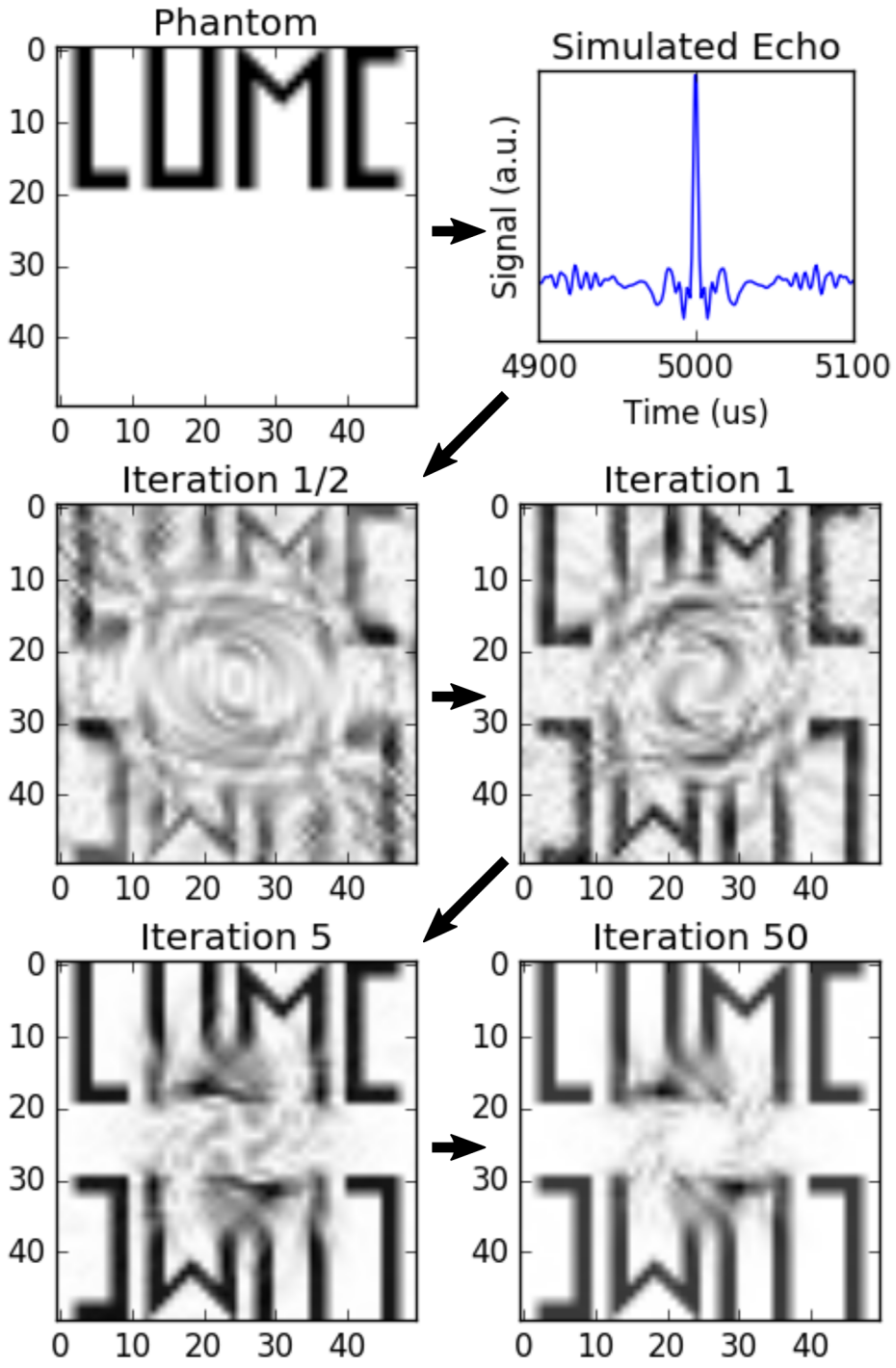

Figure 5.2: *Results from our simulated reconstruction. First, the phantom is used to calculate the echo we expect to measure. After that, the original image is reconstructed with aliasing in 50 iterations.*

Version of June 15, 2018– Created June 15, 2018 - 16:52

within the image is too large for our receive coils. Next, no noise was added to the simulated echo. This is also not realistic, since our system is limited by low SNR. How we can solve these issues, is discussed in the next chapter.

Finally, it is important to mention that the field distribution of our magnet is not optimal for rSEM encoding. When using a perfect linear gradient as encoding field, the image can (under noiseless conditions) be reconstructed without aliasing or visible blurring.

Chapter 6

Future considerations

In this chapter, we discuss the possible directions this research can take on the short and long term. First, the performance of our current setup does not yet meet the requirements for 2D imaging. However, with some minor changes, 2D imaging is within reach. These aspects are discussed in the sections on increasing SNR, broadband detection and improved magnetic field. From there on forward, we discuss long-term considerations that will eventually lead to a 3D scanner.

6.1 Increasing SNR

The largest enemy of any low-field scanner is the SNR. As discussed in section 4.4, the internal noise of the SpinCore card makes reaching the theoretical noise floor impossible. At the time of writing, though, we began measuring with a Kea^2 NMR Spectrometer Console * and first results seem to indicate a significant increase in SNR.

We do not plan on using either pre-polarisation or hyperpolarisation methods to boost SNR in the future. We believe a large enough SNR can be achieved by simply optimising our current setup and using the reconstruction methods that are being developed by our partners at the TU Delft.

*Magritek Ltd, New Zealand and Germany, `http://www.magritek.com/products/kea/`

6.2 Improving coils: broadband detection and multiple channels

One of our first steps will be the move from a single detection channel to multiple detection channels. We will first try to employ multiple surface coils that envelop the sample, similar to work by Cooley *et al.* [10]. These coils will serve to remove the aliasing from the reconstructed images and supply additional spatial information. Moreover, each coil will have improved SNR in the sample region close to it, because of the smaller size of the coils and closer proximity.

Second, we have seen that in our current magnet, our low-loss receive coils are sensitive only in a fraction of the entire region of interest, because of their limited bandwidth. As we improve the homogeneity of our magnet, the coils will cover a larger region. However, we do not expect to reduce inhomogeneity to the typical 20 kHz of coil bandwidth. We need a solution to cover the entire region of interest.

One idea would be to implement dynamic coil tuning. This could be done by using a tuning circuit that uses variable capacitor (varactor) diodes, which has been demonstrated before in MRI [37, 38]. These diodes have a capacitance in the RF-regime that depends on the DC current that flows through them. Buisman *et al.* have proposed circuits with varacter diodes that respond to an applied bias voltage in a linear way [39]. A DC voltage regulated by a computer could then automatically and rapidly scan the tuning capacitance value and thus the resonance frequency of the coil to be able to recieve signal from a larger region.

6.3 Improving our magnetic field

The homogeneity of our B_0 field will have to be increased if we want to use these varactor-based receive coils. A smaller bandwidth of Lamor frequencies would also reduce the power required to flip all spins. Finally, a higher homogeneity would also mean a larger T_2^* time. Because our sampling rate is limited, a longer echo means we can collect more data points and thus more information about the sample.

Increasing homogeneity is done by using either slightly different magnet placing or adding additional (smaller) magnets, a process called shimming, which is common practice in commercial MRI systems.

Cooley *et al.* find a reduction of about 50% of the magnetic field variation within their FOV with additional magnet shimming [10]. In a more

recent paper, they study improving the homogeneity by using a partially filled Halbach array [40]. Three concentric Halbach cylinders were filled slot-by-slot with either a strong magnet, a weak magnet or no magnet. The distribution was determined by using a genetic algorithm, constrained by a minimum field strength, whilst trying to minimise inhomogeneity. They show a 90% reduction of inhomogeneity in a $20\times20\times20$ FOV to $1.3 \cdot 10^4$ ppm.

Many more designs can be imagined, as is the subject of several theses [14, 15, 20]. One other constraint that has to be kept in mind is the weight of the total setup. Although high field homogeneity is achievable with permanent magnets[†], it comes at the cost of heavy weight.

Besides increasing the homogeneity, there is another property of our magnet that can be improved upon. As explained in section 5.2, the local minimum of our magnetic field causes the rSEM reconstruction to blur in the centre. Similar simulations that used a field with a perfect linear gradient did not show this effect. Thus it may be a good idea to choose a field distribution that does not have a local minimum at the centre of rotation.

6.4 Effects of temperature

In the further development, we will have to introduce a system that records and compensates for temperature change. Temperature influences our setup mainly through the changing strength of our permanent magnets. Increasing the temperature means the magnetisation decreases.

From existing work, we can estimate the change of Lamor frequency we will have to deal with. Moritz reports a drift of -0.0021 T/°C for the remanence of their NbFeB magnets at room temperature, at a remanence of about 1.4 T. Cooley *et al.* find a variation of 1.6 kHz/hour (0.4 °C temperature change), which corresponds to a $1.2 \cdot 10^{-4}$ fractional change in remanence, which matches closely to $1.5 \cdot 10^{-4}$ found by Moritz by measuring individual magnets.

On-site, in a Sub-Saharran developing country, our device has to be able to operate within a temperature range that could easily exceed 10°C. This would correspond to over 10 kHz of frequency change. We need a rSEM that is functional though the entire temperature range. Additionally, our coils need to be able to adapt to this new resonance frequency.

[†]See for example the commercial 0.4 T system APERTO Lucent O5 by Hitachi Medical Systems.

Whatever the solution, we will always need a system that logs the temperature accurately during each measurement.

6.5 3D imaging

As we have described previously, we plan to use a combination of frequency-encoding and rotation to obtain 2D information of our sample. It is not clear how this method should be extended into the third dimension. In this section, we describe two methods that could be used to enable imaging in three dimensions. We do not discuss gradient coils, because we want to try to eliminate these and the complications they bring along from the setup.

Transmit array spatial encoding (TRASE) [41] is a new encoding method that removes the need for gradient coils by making use of purpose-designed transmit coils and pulse sequences. The essence is that the k-space is traversed by using the phase distribution of the B_1 field over the sample, and not a B_0 field gradient.

Mathematically, both of these approaches result in the same effect. To see this, consider the magnetisation resulting from a homogeneous B_1 excitation on a B_0 field followed by a gradient along the x-direction, as is the case in traditional gradient encoding:

$$M = M_0 e^{i\phi(x)} = M_0 e^{i\gamma \Delta B_0 (\Delta t) x},$$

where γ is the gyromagnetic ratio, ΔB_0 is the B_0 gradient and Δt is the gradient duration. For a linear B_1 phase gradient (while having a homogeneous B_1 amplitude) on a homogeneous B_0 field, we have:

$$M = M_0 e^{i\phi(x)} = M_0 e^{ikx},$$

where k is the phase gradient along the sample. We see the two different hardware approaches give the same resulting magnetisation.

However, one important difference still remains. While the phase per distance for a B_0 gradient, $\gamma \Delta B_0 \Delta t$, can be varied continuously by tuning the gradient currents, the phase gradient of the transmit coil, k, is a property of the coil geometry and thus a constant. This problem was overcome by using a spin echo pulse train and two transmit coils with different phase gradients. The idea is to alternatingly send a refocusing pulse with one of the two coils. Were their phase gradients the same, the gradients would cancel out after each pair of recovery pulses. By choosing two different gradients, the magnetisation is still recovered after each pulse pair,

while the magnetisation phase gradient obtains a net increase. In this way, *k*-space can be traversed. The TRASE imaging method has been demonstrated in 1D [41] and 2D [41, 42].

These demonstrations were performed in highly homogeneous B_0 fields and are thus not directly applicable in the inhomogeneous low fields of portable scanners. Stockmann *et al.* [43] altered the TRASE scheme to be of use in inhomogeneous fields. To do this, they first exchanged hard pulse excitations for frequency-swept pulses, so called WURST pulses [44]. These pulses have a favorable frequency spectrum, which comes at the price of a longer pulse duration. Additionally, they developed a pulse sequence and processing method to account for additional phase gradients that arise when using frequency-swept pulses. They use these to demonstrate 1D imaging over a 30 kHz FOV.

The TRASE method could possibly be used to encode the third dimension in our setup. That would require two phase gradient transmit coils and at least one separate receive coil, in addition to the magnet being able to rotate around the sample. However, the long pulse durations in combination with long pulse trains means this requires a lot of power. A first step in further research would be to estimate the power required.

Additionally, the third degree of freedom could be included by moving parts of the permanent magnet array to change the magnetic field. Consider, for example, two nested dipole Halbach arrays. The field inside of the rings is a superposition of both fields and can be almost completely canceled our if the two rings have opposite orientation. When having the same orientation, the fields add up constructively. Barghoorn reports on a simulation that demonstrates this [14]. This particular example has been applied in a flow meter based on NMR that is produced by Krohne Altometer [45]. However, there are many more possibilities imaginable and we want to explore these for a potential 3D encoding technique.

Chapter 7

Conclusions

In this thesis, we have described the first measurements done with an early-stage prototype MRI scanner that is low-cost and portable. The motivation for this project is to make MRI available in developing countries.

We have described a setup for NMR in a permanent magnet array with head-sized bore and inhomogeneous, low-strength field. This setup can operate in tranceive and two-coil mode. In the tranceive setup, we use a passive switch based on crossed diodes that protects readout equipment during transmit.

Next, we demonstated spin echo measurements in this setup. We determined flip angle versus amplitude. Tranceive mode achieves a higher SNR here, mostly because we can operate it at shorter flip pulse duration and thus larger bandwidth. In general, our amplifier output power limits the bandwidth we can excite with a hard pulse. A CPMG sequence is demonstrated as well. From the decay of the intensity of subsequent echoes, we found T_2 times of 240 and 93 ms for water and oil, respectively. The observed echo shape and intensity for different coils can mostly be understood from theory. However, a quantitative calculation predicted flip angles that are a lot higher than observed values, which is likely because we are overestimating the resonance quality of our circuits.

A short noise analysis showed that the internal noise of our analogue-to-digital interface (Radioprocessor-G) contributes more than coil noise, showing that we may benefit from a new system. An estimate of coil noise hints that we have not reached the theoretical Nyquist noise lower limit, but are approximately a factor 4 higher, indicating an SNR gain might be achieved by further optimisation of electronics. We found the Faraday cage is essential in making the NMR signal visible.

In the near future, we want to perform 2D imaging using a rotating spa-

tially encoding magnetic field (rSEM). We performed a first simulation of this imaging method, which shows that our current magnetic field could function as a rSEM. At the time of writing, the first experimental tests of 2D imaging are being performed.

We described several possible hardware upgrades. To make excitation of the entire FOV possible, we need to decrease magnetic field variation. To do this, we need to redesign the Halbach array and use additional shimming magnets. Also, we either need to increase amplifier power or use frequency sweeps of excitation to scan the entire FOV. With respect to coils, we want to move from volume receive coils to multiple surface coils. Finally, we mentioned two possible approaches to extending to 3D imaging.

It is our aim to develop this prototype into a fully-functioning scanner in just a few years. Designs and computer code will all become available open-source and it is our hope this scanner can soon after be put to good use.

7.1 Acknowledgements

Several people contributed to this work. First, it was built on work by Jelle Hockx, Koen van Deelen and Wico Breimer. Wico Breimer and Tom O'Reilly were involved in the experimental work. Thomas Ruytenberg and Wyger Brink provided useful advice on several occasions. Wouter Teeuwisse was of great help in building the setup. Prof Andrew Webb gave direction and input to the project, while also helping in day-to-day experiments and counseling where needed.

We thank Martin van Gijzen, Rob Remis en Merel de Leeuw den Bouter from the TU Delft for their input and useful discussions. The magnet array was designed by Lennart Middelplaats and the RF amplifier was designed and built by Danny de Gans, both at the TU Delft.

Bibliography

[1] Driss Cammoun, Kathleen A. Davis, and William R. Hendee. Clinical Applications of Magnetic Resonance Imaging—Current Status. *Western Journal of Medicine*, 143(6):793–803, December 1985.

[2] Benjamin C. Warf. Educate One to Save a Few. Educate a Few to Save Many. *World Neurosurgery*, 79(2, Supplement):S15.e15–S15.e18, February 2013.

[3] Ryan T. Muir, Shelly Wang, and Benjamin C. Warf. Global surgery for pediatric hydrocephalus in the developing world: a review of the history, challenges, and future directions. *Neurosurgical Focus*, 41(5):E11, November 2016.

[4] Steffen Lother, Steven J. Schiff, Thomas Neuberger, Peter M. Jakob, and Florian Fidler. Design of a mobile, homogeneous, and efficient electromagnet with a large field of view for neonatal low-field MRI. *Magnetic Resonance Materials in Physics, Biology and Medicine*, 29(4):691–698, August 2016.

[5] Mathieu Sarracanie, Brandon D. Armstrong, Jason Stockmann, and Matthew S. Rosen. High speed 3d overhauser-enhanced MRI using combined b-SSFP and compressed sensing: 3d OMRI Using b-SSFP and Compressed Sensing. *Magnetic Resonance in Medicine*, 71(2):735–745, February 2014.

[6] Mathieu Sarracanie, Cristen D. LaPierre, Najat Salameh, David E. J. Waddington, Thomas Witzel, and Matthew S. Rosen. Low-Cost High-Performance MRI. *Scientific Reports*, 5:15177, October 2015.

[7] M. Packard. Proton gyromagnetic ratio. *Physical review*, 93:941, 1954.

[8] Josh Harper. *Sustainable MRI for the Developing World*. PhD proposal, Pennsylvania State University, 2017.

[9] Clarissa Zimmerman Cooley. *Portable low-cost magnetic resonance imaging*. PhD thesis, Massachusetts Institute of Technology, 2014.

[10] Clarissa Zimmerman Cooley, Jason P. Stockmann, Brandon D. Armstrong, Mathieu Sarracanie, Michael H. Lev, Matthew S. Rosen, and Lawrence L. Wald. Two-dimensional imaging in a lightweight portable MRI scanner without gradient coils: Lightweight MRI Scanner without Gradient Coils. *Magnetic Resonance in Medicine*, 73(2):872–883, February 2015.

[11] Zhi Hua Ren, Luc Maréchal, Wan Luo, Jiasheng Su, and Shao Ying Huang. Magnet array for a portable magnetic resonance imaging system. In *RF and Wireless Technologies for Biomedical and Healthcare Applications (IMWS-BIO), 2015 IEEE MTT-S 2015 International Microwave Workshop Series on*, pages 92–95. IEEE, 2015.

[12] Zhi Hua Ren, Sergei Obruchkov, Dong Wei Lu, Robin Dykstra, and Shao Ying Huang. A Low-Field Portable Magnetic Resonance Imaging System for Head Imaging. Singapore, November 2017.

[13] Dong Wei Lu and Shao Ying Huang. A TSVD-based Approach for Flexible Spatial Encoding Strategy in Portable Magnetic Resonance Imaging (MRI) System. Singapore, November 2017.

[14] Antonia Barghoorn. Halbach Magnet Array Design for Low Cost Magnetic Resonance Imaging. Master's thesis, Berlin Ultrahigh Field Facility, Berlin, 2015.

[15] Raphael Moritz. Development and characterization of Halbach arrays tailored for magnetic resonance at low magnetic field strengths. Master's thesis, Berlin Ultrahigh Field Facility, Berlin, 2017.

[16] M.S. Wijchers. Image Reconstruction in MRI: The Possibilities of Portable, Low-cost MRI Scanners. Master's thesis, TU Delft, Delft, 2016.

[17] Merel de Leeuw den Bouter. Image reconstruction in low-feld MRI: A super-resolution approach. Master's thesis, Delft University, Delft, 2017.

[18] Lukas Winter, Haopeng Han, Antonia Barghoorn, Werner Hoffmann, Stefan Hetzer, Simone Winkler, Larry Wald, Andrew Webb, Peter Blümler, and Thoralf Niendorf. Open Source Imaging Initiative. In *Proc Intl Soc Mag Reson Med*, volume 3638. ISMRM, 2016.

[19] Jelle Hockx. Designing and characterizing a hardware and software acquisition system for low field MRI -Version 5. Master's thesis, Leiden University, Leiden, 2017.

[20] Koen van Deelen. Low Field MRI Using Halbach Ferromagnet Arrays. B.S. Thesis, Leiden University, Leiden, 2017.

[21] Giulio Giovannetti, Vittorio Viti, Vincenzo Positano, Maria Filomena Santarelli, Luigi Landini, and Antonio Benassi. Magnetostatic simulation for accurate design of low field MRI phased-array coils. *Concepts in Magnetic Resonance Part B: Magnetic Resonance Engineering*, 31B(3):140–146, August 2007.

[22] Qing X. Yang, Jinghua Wang, Xiaoliang Zhang, Christopher M. Collins, Michael B. Smith, Haiying Liu, Xiao-Hong Zhu, J. Thomas Vaughan, Kamil Ugurbil, and Wei Chen. Analysis of wave behavior in lossy dielectric samples at high field. *Magnetic Resonance in Medicine*, 47(5):982–989, May 2002.

[23] Manushka V. Vaidya, Christopher M. Collins, Daniel K. Sodickson, Ryan Brown, Graham C. Wiggins, and Riccardo Lattanzi. Dependence of b_{1-} and b_{1+} field patterns of surface coils on the electrical properties of the sample and the mr operating frequency. *Concepts in Magnetic Resonance Part B: Magnetic Resonance Engineering*, 46(1):25–40, February 2016.

[24] M. E. Hayden, C. P. Bidinosti, and E. M. Chapple. Specific absorption rates and signal-to-noise ratio limitations for MRI in very-low magnetic fields. *Concepts in Magnetic Resonance Part A*, 40A(6):281–294, November 2012.

[25] D. I Hoult and R. E Richards. The signal-to-noise ratio of the nuclear magnetic resonance experiment. *Journal of Magnetic Resonance (1969)*, 24(1):71–85, October 1976.

[26] Joël Mispelter, Mihaela Lupu, and André Briguet. *NMR probeheads for biophysical and biomedical experiments*. Imperial College Press, London, 2006.

[27] Nadine Barrie Smith and Andrew Webb. *Introduction to Medical Imaging*. Cambridge University Press, 2011.

[28] M. Robin Bendall, Alan Connelly, and Jamie M. McKendry. Elimination of coupling between cylindrical transmit coils and surface-receive coils for in vivo NMR. *Magnetic Resonance in Medicine*, 3(1):157–163, February 1986.

[29] Klaus Halbach. Design of permanent multipole magnets with oriented rare earth cobalt material. *Nuclear instruments and methods*, 169(1):1–10, 1980.

[30] H. Raich and P. Blümler. Design and construction of a dipolar Halbach array with a homogeneous field from identical bar magnets: NMR Mandhalas: Design of a Dipolar Halbach Array. *Concepts in Magnetic Resonance Part B: Magnetic Resonance Engineering*, 23B(1):16–25, October 2004.

[31] David J. Griffiths. *Introduction to Electrodynamics*. Pearson Education, 4 edition, 2013.

[32] H. Y. Carr and E. M. Purcell. Effects of Diffusion on Free Precession in Nuclear Magnetic Resonance Experiments. *Physical Review*, 94(3):630–638, May 1954.

[33] S. Meiboom and D. Gill. Modified Spin-Echo Method for Measuring Nuclear Relaxation Times. *Review of Scientific Instruments*, 29(8):688, December 1958.

[34] P. C. Lauterbur. Image Formation by Induced Local Interactions: Examples Employing Nuclear Magnetic Resonance. *Nature*, 242(5394):190–191, March 1973.

[35] Z. H. Cho, S. T. Chung, J. Y. Chung, S. H. Park, J. S. Kim, C. H. Moon, and I. K. Hong. A new silent magnetic resonance imaging using a rotating DC gradient. *Magnetic Resonance in Medicine*, 39(2):317–321, February 1998.

[36] Richard Gordon, Robert Bender, and Gabor T. Herman. Algebraic Reconstruction Techniques (ART) for three-dimensional electron microscopy and X-ray photography. *Journal of Theoretical Biology*, 29(3):471–481, December 1970.

[37] Jean Rousseau, Pascal Lecouffe, and Xavier Marchandise. A new, fully versatile surface coil for MRI. *Magnetic Resonance Imaging*, 8(4):517–523, January 1990.

[38] L. Tugan Muftuler, Gultekin Gulsen, Kumsal D. Sezen, and Orhan Nalcioglu. Automatic Tuned MRI RF Coil for Multinuclear Imaging of Small Animals at 3t. *Journal of Magnetic Resonance*, 155(1):39–44, March 2002.

[39] K. Buisman, L.C.N. de Vreede, L.E. Larson, M. Spirito, A. Akhnoukh, T.L.M. Scholtes, and L.K. Nanver. Distortion-free varactor diode topologies for RF adaptivity. In *IEEE MTT-S Int. Microw. Symp. Dig.*, 2005.

[40] Clarissa Zimmerman Cooley, Melissa W. Haskell, Stephen F. Cauley, Charlotte Sappo, Cristen D. Lapierre, Christopher G. Ha, Jason P. Stockmann, and Lawrence L. Wald. Design of Sparse Halbach Magnet Arrays for Portable MRI Using a Genetic Algorithm. *IEEE Transactions on Magnetics*, pages 1–12, 2017.

[41] Jonathan C. Sharp and Scott B. King. MRI using radiofrequency magnetic field phase gradients. *Magnetic Resonance in Medicine*, 63(1):151–161, January 2010.

[42] Jonathan C. Sharp, Scott B. King, Qunli Deng, Vyacheslav Volotovskyy, and Boguslaw Tomanek. High-resolution MRI encoding using radiofrequency phase gradients. *NMR in Biomedicine*, 26(11):1602–1607, November 2013.

[43] Jason P. Stockmann, Clarissa Z. Cooley, Bastien Guerin, Matthew S. Rosen, and Lawrence L. Wald. Transmit Array Spatial Encoding (TRASE) using broadband WURST pulses for RF spatial encoding in inhomogeneous B 0 fields. *Journal of Magnetic Resonance*, 268:36–48, July 2016.

[44] Luke A. O'Dell. The WURST kind of pulses in solid-state NMR. *Solid State Nuclear Magnetic Resonance*, 55-56:28–41, October 2013.

[45] Marco Leendert Zoeteweij, Olaf Jean Paul Bousché, Cornelis Johannes Hogendoorn, Ariël De Graaf, Jan Teunis Aart PORS, and Jan-Willem Ramondt. Nuclear magnetic flowmeter, 2016. US Patent US9429456B2, assigned to Krohne AG.